Title
A microfabricated, optically accessible device to study the effects of mechanical cues on collagen fiber organization

Journal
Biomedical Microdevices, 16(2)

ISSN
1387-2176

Authors
Winkler, Moritz
Simon, Melinda G
Vu, Timothy
et al.

Publication Date
2014-04-01

DOI
10.1007/s10544-013-9829-x

Peer reviewed

HHS Public Access

Author manuscript

Biomed Microdevices. Author manuscript; available in PMC 2018 April 26.

Published in final edited form as:

Biomed Microdevices. 2014 April ; 16(2): 255–267. doi:10.1007/s10544-013-9829-x.

A microfabricated, optically accessible device to study the effects of mechanical cues on collagen fiber organization

Moritz Winkler,
Department of Biomedical Engineering, 3120 Natural Sciences II, University of California, Irvine, CA 92697, USA

Gavin Herbert Eye Institute, University of California, Irvine, 843 Health Sciences Road, Hewitt Hall, Room 2036, Irvine, CA 92697-4390, USA

Melinda G. Simon,
Department of Biomedical Engineering, 3120 Natural Sciences II, University of California, Irvine, CA 92697, USA

Timothy Vu,
Department of Biomedical Engineering, 3120 Natural Sciences II, University of California, Irvine, CA 92697, USA

Trevor L. Gartner,
Department of Biomedical Engineering, 3120 Natural Sciences II, University of California, Irvine, CA 92697, USA

James V. Jester,
Department of Biomedical Engineering, 3120 Natural Sciences II, University of California, Irvine, CA 92697, USA

Gavin Herbert Eye Institute, University of California, Irvine, 843 Health Sciences Road, Hewitt Hall, Room 2036, Irvine, CA 92697-4390, USA

Abraham P. Lee, and
Department of Biomedical Engineering, 3120 Natural Sciences II, University of California, Irvine, CA 92697, USA

Donald J. Brown
Gavin Herbert Eye Institute, University of California, Irvine, 843 Health Sciences Road, Hewitt Hall, Room 2036, Irvine, CA 92697-4390, USA

Abstract

Correspondence to: Donald J. Brown.

Moritz Winkler and Melinda G. Simon these authors contributed equally to this manuscript

This study has been presented in part at the International Society for Eye Research Biannual Meeting in Berlin, July, 2012.

No conflicting relationship exists for any author.

Ethics statement

All animal work was performed in accordance with the ARVO guidelines for the use of animals in ophthalmic and visual research.

As the primary structural protein of our bodies, fibrillar collagen and its organizational patterns determine the biomechanics and shape of tissues. While the molecular assembly of individual fibrils is well understood, the mechanisms determining the arrangement of fibers and thus the shape and form of tissues remain largely unknown. We have developed a cell culture model that successfully recapitulates early tissue development and the *de novo* deposition of collagen fibers to investigate the role of mechanical cues on collagen fiber alignment. The devices used a thin, collagen-coated deformable PDMS membrane inside a tissue culture well built on microscope-grade coverslips. Deformations and strains in the PDMS membrane were quantified by tracking fluorescent bead displacement and through the use of a COMSOL model. Cyclical strains were applied to serum-cultured rabbit corneal cells at 0.5 Hz for 24–48 h and showed a preferred alignment after 36 h of cyclical loading. Cells cultured with ascorbic acid under methylcellulose serum-free conditions deposited a collagenous matrix that was visible under live second harmonic generation microscopy at week 4. Our microfabricated tissue culture system allows for the controllable application of a wide range of stress profiles to cells, and for the observation and quantification of cells and de novo collagen formation *in vitro*. Future studies will involve the fabrication of models to study the formation and organization of collagen in ocular diseases.

Keywords

Mechanome; Cornea; Collagen; Corneal keratocytes; Biomechanics; Second harmonic generation imaging; Microfluidics

1 Introduction

Collagen, a mechanically strong fibrous protein, is the main structural element in animals. Collagen molecules assemble as fibrils that aggregate into larger fibers, which give form and shape to tissues necessary for proper organ function. The importance of collagen organization is perhaps most pronounced in the vertebrate eye. Here, collagen fibers form tissues that serve both as part of the protective outer tunic and as the major refractive element of the ocular system, i.e. the cornea. The cornea consists primarily of a highly organized collagenous matrix that is both transparent and mechanically stable. To fulfill its function as an optical lens, the cornea must maintain a specific parabolic shape that is different from the rest of the eye, which allows light to be focused back to the retina. This shape is thought to be controlled by the mechanical properties of collagen and its 3-dimensional structural organization (Winkler et al. 2011). During ocular development, the forces exerted by intraocular pressure (IOP) on the cornea and sclera drive the development of corneal curvature (Rabinowitz 1998; Kamotani et al. 2008; Moraes et al. 2009, 2011, 2013), and depriving the developing chick eye of these forces has been shown to result in a lack of differentiation in curvature between cornea and sclera (Coulombre and Coulombre 1958). While much is known regarding the molecular mechanisms controlling collagen fibril assembly (Benedek 1971; Coulombre and Coulombre 2005; Cox et al. 1970; Maurice 1957), the mechanisms determining corneal and tissue shape and the macro-structural organization of collagen are largely unknown (Ruberti and Zieske 2008).

Mechanical forces have been repeatedly shown to play an important role in directing cell differentiation (McBeath et al. 2004; Palomares et al. 2009; Arnsdorf et al. 2009; Wang et al. 2003a) and cell morphology (Eastwood et al. 1998; Wang et al. 2003b), as well as upregulate collagen synthesis (MacKenna et al. 2000; Screen et al. 2005; Kim et al. 1999) and impact macrostructural collagen fiber organization (Gupta and Grande-Allen 2006; Karamichos et al. 2007). Mechanical loading has also been used to strengthen and enhance engineered tissue constructs (Case et al. 2003; Duty et al. 2007; Butler et al. 2009; Nirmalanandhan et al. 2008). These studies used a variety of approaches to load cells and collagenous matrices, many of which have been reviewed recently (Moraes et al. 2011; Quinlan et al. 2011). In these systems, strain was applied uniaxially or biaxially. In the uniaxial configuration, a substrate is generally fixed at two locations and distended, either by increasing the distance between the endpoints, or by applying negative pressure (vacuum) (Lee et al. 2007). On the other hand, biaxial strain devices produce a distribution of strain values in 2 dimensions, typically described as radial and circumferential strain, by distending the membrane using a piston, vacuum pressure, or positive fluid pressure. Depending on the method used to induce strain, the circumferential strain may be either uniform or non-uniform and cells may experience significant compression along a secondary, perpendicular axis. While uniaxial strain is easier to implement and calculate, biaxial strain devices provide a more physiologically-relevant model for the strain distributions experienced by cells *in vivo*.

When seeding cells onto an existing extracellular matrix, such as a collagen hydrogel, the influence of topographical cues must also be taken into account, as they have been shown to override mechanical cues (Saeidi et al. 2012). Collagen fiber organization in these systems is due to a remodeling of the existing collagen rather than the generation of a *de novo* organized matrix. To accurately recapitulate early tissue development, model systems must support cells that are capable of generating a collagenous matrix for extended periods of time to allow for the synthesis of sufficient amounts of collagen fibers for imaging studies.

Microfabricated systems for the study of cell response to biaxial mechanical strain over short periods of time have been demonstrated previously by other groups (Kamotani et al. 2008; Moraes et al. 2013). In these devices, cell viability may be maintained over the course of no more than 2 days (Kamotani et al. 2008; Moraes et al. 2009) however, the remodeling and *de novo* formation of collagen requires several weeks (Ruggiero et al. 1996). Assessing the effects of mechanical forces on *de novo* collagen fiber organization thus requires a system that (1) is capable of supporting cell attachment on a deformable substrate, (2) maintains cell viability long-term, (3) supports formation of a *de novo* collagenous matrix, (4) can apply biaxial mechanical loads within a physiological range controllably and repeatedly, and which (5) is compatible with a variety of optical imaging modalities that allow for live cell imaging.

In this paper, we demonstrate a biaxial strain device and techniques capable of sustaining cell cultures that promote *de novo* generation of a collagenous extracellular matrix over the course of several weeks, and to test the hypothesis that a *de novo* synthesized collagen matrix is assembled along primary lines of stress. In addition, the application of cyclic biaxial strain to the devices induces alignment of cells. This achievement required the

development of a procedure to coat PDMS devices with collagen, and determination of a proper cell seeding density to maintain an appropriate cell density throughout the duration of the culture period.

2 Materials and methods

2.1 Design

The microfabricated devices consisted of a two layer device made from the silicone rubber polydimethylsiloxane (PDMS), mounted onto a circular glass cover slip for imaging (Fig. 1). The thin bottom layer of the PDMS device comprised a membrane for cell attachment and mechanical loading, and a fluidic channel through which pressure was applied. A thicker layer of PDMS was bonded to the top of this bottom layer, to provide a handle to remove the PDMS membrane from the mold. This thick layer also served as a 12 mm diameter tissue culture well to contain the cell culture media atop the PDMS membrane. A microchannel extending from either side of the membrane allowed the application of pressure to the membrane through the inlet hole. An outlet hole was also used to facilitate filling of the device with fluid without the application of high pressure to the PDMS thin membrane. After filling, the outlet hole was closed. Filling of the device with fluid rather than air allowed for long-term pressurization experiments incompatible with the gas permeability of PDMS.

2.2 Fabrication

Devices were fabricated with PDMS (Sylgard 184, Dow Corning) using multi-layered soft lithography methods (Li et al. 2005). A mold for soft lithography was prepared using SU-8 photoresist (Microchem, Newton, MA). Device features on the finished mold were 100 μm high.

Following the preparation of the mold, PDMS tissue culture membranes were created. Five grams of PDMS, mixed in a ratio of 20:1 precursor: curing agent (w/w) were poured onto the SU-8 mold and spun at 300 rpm for 5 min, resulting in a 100 μm PDMS thin-film. This film was then baked on the mold for 30 min at 120 °C to create the deformable membrane. During baking, a previously prepared, 4 mm-thick slab of cured PDMS (mixed in a 10:1 ratio of precursor:curing agent) was cut to the appropriate size and a 12 mm diameter hole was bored into this slab using a biopsy punch. This layer formed a 12 mm diameter tissue culture well surrounding the flexible membrane, which had a diameter of 10 mm, and provided space for up to 700 μL of cell culture media. Once the thin PDMS film was baked, the thick layer of PDMS was irreversibly bonded to the thin membrane after treating both pieces with oxygen plasma at 200 mTorr for 2 min (Harrick Plasma, Inc.). Following this bonding step, the device was baked in a 60 °C oven for at least 3 h. After this baking step, the device was cut from the mold and removed, using the thick PDMS layer as a handle for this process. 500 μm diameter inlet and outlet holes were bored in the device, using a blunt syringe needle. These holes allowed for pressure to be applied to the underside of the PDMS membrane during testing. Finally, the released device was then bonded to a circular glass cover slip by treatment with oxygen plasma.

Finished devices underwent one last baking step at 120 °C for 24 h. A final plasma treatment was administered to render the surface of the PDMS membrane hydrophilic. Then, 100 μL of bovine type I collagen (Advanced Biomatrix, San Diego, CA) at 3.1 μg/μL was pipetted onto the PDMS membrane. The collagen solution was allowed to incubate for at least 2 h, facilitating attachment of collagen to the activated PDMS surface. Following collagen incubation, the solution was washed away using sterile phosphate buffered saline solution (PBS) and the devices were sterilized by overnight exposure to UV light before cell seeding.

2.3 Characterization

Polystyrene beads with 1 μm diameter were suspended in 70 % EtOH and pipetted onto the device to create a thin film of beads on the membrane. After evaporation of the residual ethanol, the beads remained in place on the membrane and could be used to track membrane displacement after deflection, as demonstrated in previous studies (Moraes et al. 2010). The beads were illuminated with a HeNe laser at 543 nm and fluorescent signals acquired using the Zeiss 510 LSM in confocal mode.

To precondition the devices, cyclical pressure was applied at 0.5 Hz for 10 min. Devices were then pressurized by injecting deionized water using a programmable pump (Harvard Apparatus, Holliston, MA). Consecutive overlapping z-stacks were acquired, covering an area of about 0.9 mm by 6 mm that included the center of the membrane as well as the periphery, before increasing the injection volume and scanning again. The positions of the fluorescent beads at each step were marked in Amira 5.4 (Visual Sciences Group, Burlington, MA) using the Landmark feature and 3-D coordinate sets were exported to Microsoft Excel 2010.

Because on our devices cells were cultured atop the membrane rather than inside a 3-D scaffold, they were mechanically isolated from internal membrane stresses. However, as the membrane expanded, cells were stretched and displaced. The stretch acting on cells was characterized by two main components: radial stretch t_r and circumferential stretch t_c. The ratio of circumferential to radial stretch as well as their magnitudes was calculated as a function of distance from the center of the membrane (Appendix A).

2.4 Finite element model

A finite element model of the device was created in COMSOL Multiphysics 4.3 (COMSOL Inc., Burlington, MA). Great care was taken to accurately model the membrane, however the surrounding geometry was simplified to reduce computational load, as it was deemed unlikely to have a measurable effect on membrane deformation. Mesh quality was manually adjusted to ensure a balance between simulation accuracy and computation time. 3-D and 2-D plots were generated from the simulation data to visualize stresses and device deflection. Numerical deformation values were exported and plotted in Microsoft Excel and compared to membrane displacement measured using fluorescent beads.

2.5 Cell culture

Rabbit eyes were procured from Pel-Freez (Rogers, AK) and primary corneal cells were harvested following previously established protocols (Jester and Ho-Chang 2003). Cells

were plated on the devices at a density of 15,000/cm^2 and placed in an incubator for 4 h to allow cell attachment. Successful attachment was confirmed using phase contrast microscopy. Cells were cultured on devices with Dulbecco's modified Eagle's minimum essential medium with pyruvate (DMEM; Invitrogen, Carlsbad, CA) either supplemented with 10 % fetal bovine serum for cell alignment studies or serum-free DMEM supplemented with non-essential amino acids (Life Technologies, Waltham, MA) and ascorbic acid (Sigma-Al-drich Corp, St. Louis, MO) for collagen fiber assembly studies.

2.6 Mechanical cell stimulation

After allowing cells to adhere and spread on the device surfaces overnight, devices and cells were photographed using phase contrast microscopy to assess viability and degree of attachment. The devices were then placed back in the incubator and connected to the programmable pump that generated a cyclical inflate/deflate pattern to stretch the cells with a 2 s period for 36 h. The amount of injected fluid was calibrated to achieve a maximum stretch of less than 10 %. Following completion of the stretch cycles, cells were fixed using 2 % paraformaldehyde in PBS, and then stained with phalloidin (actin stain) and DAPI (nuclei). Membranes were removed using a 10 mm trephine, placed on microscopy slides and imaged using standard fluorescence microscopy.

2.7 Live cell microscopy

Microscopic imaging was performed on a LSM 510 confocal microscope (Carl Zeiss, Carlsbad, CA). Nonlinear optical signals were generated using a Titanium:Sapphire laser (Coherent Inc., Santa Clara, CA) with a pulse width of 150 fs. Peak wavelength was adjusted based on application and was set to 800 nm for imaging of collagen and to 760 nm for NADH cellular imaging.

Collagen fibers were imaged using Second Harmonic Generation (SHG) microscopy. This nonlinear optical imaging technique uses near infrared femtosecond laser pulses to generate frequency-doubled, visible light in an absorption-free process. Due to the nature of SHG, only structures lacking central symmetry, such as collagen fibers, will emit an SHG signal. Cells generally possess central symmetry, so the signal cancels itself out. This allows imaging of fibrillar collagen without the use of exogenous stains or dyes.

Serial 3-D image stacks were acquired using a motorized stage following previously established protocols (Winkler et al. 2011). Briefly, overlapping z-stacks were concatenated in ImageJ to form a single, large-scale mosaic that retained the sub-micron resolution of each individual image.

2.8 Fluorescence cell microscopy

Fluorescence images were acquired using a Leica DMI 6000B inverted microscope with a motorized stage using a 20×/0.7 NA objective. Overlapping images were acquired serially and stitched together to generate a large-scale 2-D image depicting the entire membrane using a custom-written journal for MetaMorph 7.8 (Molecular Devices, Sunnyvale, CA).

2.9 Image processing and analysis

Images were analyzed using an ImageJ plugin, OrientationJ (Rezakhaniha et al. 2012). Briefly, this plugin created color-coded overlays based on local orientation in addition to providing numeric orientation values. Color-coded images were then used to qualitatively assess cell orientation. Quantification of orientation was performed on images by generating a small (20 μm×20 μm) region of interest (ROI) and determining the predominant angle within that region using OrientationJ. A custom-written ImageJ script moved the ROI outwards, recording orientation values and position information to a spreadsheet. This process was repeated several times, each time offsetting the direction of travel by 15°, to collect orientation values throughout 180°. The resulting dataset then contained the predominant angle within each ROI, along with the position of each ROI in polar coordinates.

Cell orientation was then expressed by comparing the calculated orientation angle of the cells in a particular ROI with the angular (theta) component of the polar coordinates of that ROI on the membrane surface. This value was a measure of the averaged predominant cell orientation compared to the angular (θ) component of its polar coordinates as given by

$$\theta_{alignment}(r) = \frac{\sum_i |\alpha_i - \theta_i|}{\#\ of\ ROIs}$$

Where r is the radial coordinate, α_i is the predominant angle of cell orientation within each ROI, and θ_i is the polar angle coordinate of each ROI as illustrated in Fig. 6a (inset).

At the 3 o'clock position, θ=0, so cells pointing toward 3'o clock would have a $\theta_{alignment}$ of 0, while the $\theta_{alignment}$ of those pointing towards 12 o'clock would be 90°. The standard deviation, shown as error bars, became smaller if more cells are oriented in the same direction. A hypothetical perfect orientation, where all cells are oriented in the same direction, would have an error of 0, while an area with completely randomly oriented cells would have an error of ±22.5°.

3 Results

3.1 Device performance

Membrane deflection was visualized by tracking the displacement of fluorescent microbeads in 3-D using confocal microscopy (Fig. 2). In its relaxed state, the membrane was almost completely flat (red beads). With increasing pressure, the membrane deflected upward (green beads). The glass cover slide did not deflect (blue plane). The vertical deflection of the membrane can be clearly seen in the cross-sectional view (Fig. 2a) and the 3-D render (Fig. 2b). As a result of this deflection, the membrane was stretched, causing an outward displacement of beads as seen in a top-down view (Fig. 2c, d and e). The displacement, and therefore the stretch, was nonuniform across the device. Near the center and in the very periphery (Fig. 2c and e), beads experienced very little in-plane displacement, and moved almost solely in the vertical (z-) direction. Conversely, the amount of in-plane displacement

initially increased towards the periphery and reached a peak point (Fig. 2d) before decreasing again.

Corresponding views from the finite element model are found in Fig. 3. The magnitude of in-plane displacement across the membrane was visualized using a heat map (Fig. 3a and c). Hotter colors (orange, red) indicated high levels of in-plane displacement, while cooler colors (blue-green) were associated with smaller amounts of displacement. The maximum in-plane displacement (dark red), formed a ring centered at about 60 % of the distance between membrane center and periphery (Fig. 3c, arrows). Main displacement vectors were plotted in a top-down view (Fig. 3b) and showed a symmetric, concentric outward motion.

Bead displacement was assessed numerically and plotted to compare computer simulation predictions with experimental values (Fig. 4). Because the membrane deflected vertically, the amount of absolute displacement was greatest along the z-axis. In analyzing bead displacement, the z component was therefore isolated (Fig. 4a) from the in-plane or x/y displacement (Fig. 4b). To validate our Finite Element Model, the corresponding displacement values generated by the simulation are overlaid onto the plots. Both vertical and in-plane displacement values from the model correlate well with our experimental observations. Based on these values, radial and circumferential strain values were calculated (see Appendix A) and plotted as a function of radial distance (Fig. 4c).

3.2 Cell viability

Cells were exposed to two separate culture conditions. When cultured with serum, cells remained viable throughout the duration of the mechanostimulation experiments (total ~48–72 h). Due to the presence of serum, these cells continued to proliferate and cell density increased with time, restricting experiments to a maximum of 3 days to prevent overgrowth.

Conversely, when cultured with serum-free media, cells remained alive but did not proliferate. Viability was assessed visually using optical bright-field microscopy, and in the case of collagen studies using intrinsic multiphoton fluorescence imaging of NADH/FADH. Both tests showed that cells remained viable for several weeks. Cell viability of up to 6 weeks has been demonstrated (data not shown).

3.3 Cell alignment

Alignment analysis was performed on serum-cultured cells following 36 h of cyclical stretch. Figure 5a shows expected values for cell alignment. Actual cell alignment can be seen in Fig. 5b. Here, phalloidin-stained cells were imaged using fluorescence microscopy and color-coded according to their orientation using OrientationJ. The cells aligned concentrically in the periphery, but did not appear to be aligned along either the radial or circumferential direction in the membrane center. High-resolution views of individual aligned cells imaged using confocal fluorescence microscopy can be seen in Fig. 5c and d (green = phalloidin stain/actin, red = DAPI stain/nuclei).

The device was then divided into four concentric regions (Fig. 6a), and cell alignment for each region was quantified using OrientationJ. The plot in Fig. 6b shows the average deviation in degrees from the expected alignment value as seen in Fig. 6a.

In the central region, $\theta_{alignment}$ was near 45° with a high error, indicating random cell alignment. With increasing distance from the center, $\theta_{alignment}$ approached 90° and the error was markedly reduced, indicating a strong preference for an orientation nearly perpendicular to the radius vector as predicted in Fig. 5a. In the periphery, the alignment was slightly reduced.

3.4 Collagen synthesis and alignment

Primary rabbit corneal cells were cultured under serum-free conditions with ascorbic acid for 4 weeks to promote collagen formation. After week 2, weak SHG signals could be detected from the collagen, signaling the formation of collagen fibers. After week 4, a thin collagenous matrix emitted strong SHG signals (Fig. 7a). No preferential alignment of collagen fibers was visible; however the fibers did form “bubble-like” shapes around regions with no cell attachment. This uneven cell coverage may be due to bubbles that can sometimes occur as part of the collagen coating process when preparing devices for tissue culture.

Devices, cells and matrix then underwent cyclical strains for 24 h, were imaged using SHG, and then underwent a second 24 h strain cycle with subsequent imaging. The resulting images are shown in Fig. 7. Two locations were imaged: One near the center (Fig. 7b and c), and one peripherally approximately 4 mm from the device center (Fig. 7d and e). After the first 24 h, collagen alignment did not appear to have changed near the center (Fig. 7b), however the peripheral collagen showed preferential alignment in one direction. This alignment appeared to increase slightly by day 2 (Fig. 7e). After undergoing cyclical strain, the overall strength of the SHG signal had markedly decreased from the strength of the signal prior to strain application.

4 Discussion

We have developed a microfabricated device capable of recapitulating the biaxial strain conditions experienced by corneal cells during assembly of the corneal extracellular matrix. This device is compatible with virtually all common optical microscopy techniques, including nonlinear optical imaging, and allows for live cell imaging. As a low-cost, disposable system, the device can be manufactured in larger quantities with relative ease, and can be used evaluate the effects of biaxial strain on collagen fiber assembly by different cell types.

4.1 Device considerations

To enable the study of *de novo* collagen formation and its responses to cyclic biaxial strain, several developments beyond what has been presented in literature were demonstrated. The devices consisted only of glass and PDMS with a collagen coating. This allowed for sustained culture of cells for longer periods of time than previous studies (Kamotani et al. 2008; Moraes et al. 2010, 2013; Balestrini et al. 2010) which enabled the formation of collagen *de novo* by cells cultured on the devices. The large surface area of the device permitted collection of larger data sets and examination of the effects of a wide variety of strain conditions on a single device. The large surface area of the device necessitated careful

consideration of the deformation required by the membrane to mimic physiological loads, while operating within the working distance of the imaging system. Finally, the device was designed for compatibility with a second harmonic generation imaging system to enable live imaging of collagen formation, while also maintaining compatibility with conventional bright-field and confocal microscopy imaging systems.

PDMS was chosen as the material for these devices, owing to its optical transparency, proven biocompatibility, and deformability. In contrast to systems developed by other labs (Kamotani et al. 2008; Moraes et al. 2010, 2013; Balestrini et al. 2010), our device consists solely of PDMS and does not require the use of pins (Moraes et al. 2010) and a lubricant (Moraes et al. 2010) as an actuation mechanism, simplifying the fabrication and reducing the cost of using these devices. Despite these benefits, cells do not readily attach to PDMS and wouldn't adhere strongly enough to survive long-term culture or mechanical strain. To overcome this challenge, molecular collagen was incubated on the devices immediately following plasma treatment, which covalently bonded collagen on to the activated PDMS surface. With this molecular collagen coating, cells were demonstrated to survive up to periods of 6 weeks on the devices, far exceeding results of prior studies which concluded with 24 h timepoints (Kamotani et al. 2008; Moraes et al. 2010, 2013). Achieving extended cell cultures for periods of 6 weeks requires great care in maintaining sterile cell culture technique over the course of many cell media changes, in order to minimize the risk of bacterial contamination to the cells. Optimization of the cell seeding density was achieved in order to enable these longer-term studies.

In another departure from previously published studies on the use of microfabricated membranes to apply cyclic strain to cells, the area for cell culture in the devices presented here is 34–400 times the area available in previously published systems (Kamotani et al. 2008; Moraes et al. 2009). Aside from the fact that the large cell culture area in these devices mimics the area available from the chick corneal model, this feature allows for the study of more cells at once. Imaging programs enabling automated capture and stitching of images allow for the collection of larger data sets than previously available.

Finally, the design of the pressure application system for the device presented here allows for imaging of the device under strain conditions since the deflection distance of the membrane used in these studies was sufficient to induce strain for cell and collagen alignment, while also operating within the working distance of the microscope objective lens used. This feature allows for the characterization of strain profiles on the membrane surface by using fluorescent beads placed on the membrane and tracking their displacement with the application of pressure. Using this technique, combined with a stack of images obtained from confocal microscopy, 3-D positions of the beads before and after displacement were used to calculate the radial and circumferential strains across the device. The use of cyclical pressure to apply strain in this system allows for the mimicry of diurnal strain conditions or other cyclic strain patterns found in living eyes. Fabrication of the device and calculations of the strain profile on the membrane are simplified by the use of a single device material, PDMS, throughout (Moraes et al. 2013). The use of fluidic pressure to distend the membrane, rather than a system of pins (Moraes et al. 2009), further simplifies the fabrication of the device and minimizes failures due to moving parts within the device.

Enabling second harmonic generation imaging imposed size constraints on the device design. The active imaging area of the system required the device to fit on the area of a 42 mm diameter circular glass cover slip. With this consideration in mind, a device consisting of a single, 10 mm diameter stretchable cell culture area was designed, in order to maximize the available imaging area per device, while enabling the study of a wide variety of strain conditions on a single device. Fabrication of a thin (100–150 μm) PDMS membrane, suspended over such a large area required consideration of the membrane thickness and the feature size of the microfluidic channel underneath the membrane. A thin PDMS membrane suspended over an area 10 mm in diameter will experience some sagging. If sufficient sagging occurs immediately following a plasma bonding step during fabrication, the thin PDMS membrane will bond irreversibly to the glass coverslip, rendering the device useless for cell stretching experiments. Using a height of 100 μm for the microfluidic channel, combined with a PDMS membrane thickness of 100–150 μm, was sufficient in most cases to prevent this problem. To further prevent this problem, devices were incubated upside-down (glass coverslip side up) once the PDMS device was bonded to the glass coverslip, preventing gravity from aiding the sagging-induced bonding. PDMS membranes were designed to have a optimal thickness of between 100 and 150 μm in order to mitigate tearing of membranes during fabrication or actuation (which occurred when the membranes were too thin) and to prevent excessive sagging of the PDMS membrane which lead to the bonding referenced above (which occurred when the membranes were too thick). Additional consideration was given to the maximum focal depth allowed by the imaging system. The device was designed to allow application of sufficient strain to mimic physiological strain conditions, while operating within the working range of a 40×/1.1 NA water immersion objective. Using high resolution imaging modalities such as SHG and two-photon excited fluorescence enabled label-free, live imaging of collagen formation and organization, as well as imaging of cell activity by using intrinsic fluorophores. Additionally, cells can be fixed and stained using a variety of labels. For this purpose, the device is also compatible with conventional bright field and confocal microscopy systems.

4.2 Live cell studies

Primary rabbit corneal cells were exposed to two different conditions: (1) Cultured with serum, cells remained mechanically active and began to respond to mechanical stimulation within 24 h. (2) When grown under serum-free conditions, cells became biosynthetically active, assembling a collagenous matrix over the course of several weeks. Under these conditions, cells remained quiescent, and were used to test long-term viability and the potential for *de novo* collagen formation.

When applying strain to mechanically active cells, we found that they tended to align perpendicular to the dominant (radial) direction of stress, particularly in the periphery of the device. It has been proposed that this perpendicular alignment is preferred as it minimizes stress on the cells (Ruberti and Zieske 2008). This reaction to cyclical stress is notably different from experiments using static stretch, where cells aligned at ~40° relative to the direction of stress (Paten et al. 2011).

The response of mechanically active cells to cyclical load has been the subject of many studies (Dartsch et al. 1986; Dartsch and Hämmerle 1986; Wang and Thampatty 2006; Williams 1998; Kanda and Matsuda 1993; Kanda et al. 1993). There is widespread agreement that after >24 h of cyclical load, the majority of cells align along a preferential direction, whereas in the unloaded controls, cells retain random orientations. The reported angle relative to the direction of stress however varies widely. Dartsch et al. concluded that higher magnitudes of stress lead to a steeper angle (Dartsch et al. 1986), while Wang et al. reported perpendicular alignment after 10 weeks of cyclical load (Wang and Thampatty 2006). The differences in the reported values are likely due to the multitude of different factors that influence cell responses to mechanical forces. In addition to using different cell types, studies differed in the stretch frequency and magnitude, the length of the experiment, the type of load applied, and the type of substrate used. Our device represents an approach to help isolate some of these factors, since parameters such as stretch frequency and duration are easily varied.

Ruberti et al. have reported that topographical cues may override mechanical ones (Saeidi et al. 2012). To characterize the cell response to loads, mechanical cues have to be decoupled from topographical input from the substrate. The PDMS membranes used in our devices are significantly stiffer than collagen hydrogels. Moreover, the cells are seeded atop the membrane rather than inside a 3-D scaffold and are thus largely isolated from intrinsic topographical features and load-induced topographical changes which may provide alignment cues. Finally, because the membrane stretch exhibits radial symmetry, stretch thinning under uniaxial load, which is a factor especially in materials with a high Poisson's ratio, is hidden from the cells.

4.3 Future directions

The techniques of microfabrication used in this approach lend themselves to the construction of micropatterned membranes for the application of different types of strain profiles than the type of strain profile presented in this paper. Using microfabrication, a patterned membrane with two different thicknesses could be conceived. This pattern would produce a membrane with one side under lower strain, and the other side with comparatively high strain. By culturing cells atop this device, it would then be possible to observe the effects of two different strain levels on the cells or extracellular matrix simultaneously. Furthermore, the interaction between cells cultured adjacently on a surface under low- and high-values of strain could be observed.

These patterns including areas of high and low values of strain can be used as model systems for different physiological processes including simulating a developing cornea, corneal wound healing, and simulating various diseases such as keratoconus, where thinning of the cornea occurs. The biomechanics of a corneal incision for example can be mimicked by creating a membrane featuring a thin slit.

One potential application of interest in the study of the cornea is *de novo* collagen formation and remodeling in certain diseases. Keratoconus is a degenerative disease in which the cornea is stretched and thinned, and leads to vision problems which can interfere with a person's ability to lead a normal life. Using microfabrication, a membrane to mimic the

strain pattern in a thinning cornea could be developed to provide insight into the collagen remodeling processes in this disease. Compared to models such as the chick cornea, this approach would allow a great degree of control over the strain pattern induced, and provide a nearly limitless supply of devices for study.

These designs can be virtually evaluated using our finite element model, and can be altered and optimized to produce nearly any conceivable set of load conditions. Once the desired load conditions have been achieved by a specific model configuration, the final design can then be produced rapidly.

Acknowledgments

The authors wish to acknowledge financial support from the following sources: NIH grants EY07348, EY018665, EY016663, EY019719, The Discovery Eye Foundation, The Skirball Program in Molecular Ophthalmology, Support grant from Research to Prevent Blindness, Inc, and the NSF-IGERT LifeChips program at the University of California, Irvine. The authors also wish to acknowledge the contributions of Stephanie Tran and Eric Viola for their help in image processing and data analysis.

The sponsor or funding organization had no role in the design or conduct of this research.

Appendix A

Strain calculations

Circumferential strain

The circumferential component can be calculated by measuring the two-dimensional displacement from the center. All calculations for the circumferential strain therefore take place in a two-dimensional, “top down view” coordinate system, where the center of the membrane is coincident with the origin.

As the membrane deflects and stretches, all points move outward. Locations equidistant from the origin can be described as points on a circle concentric with the center of the membrane. All points on this circle move outwards by the same amount, because the radius of the circle increases. As a result, the circumference and thus the tangential distance between all points on that circle increases.

Let $\overrightarrow{\rho}_r$ be the radius vector for such a circle before inflation, and $\overrightarrow{\rho}'_r$ be the radius vector for the circle after inflation. Due to the outward motion of points in response to inflation, $\left|\overrightarrow{\rho}'_r\right| > \left|\overrightarrow{\rho}_r\right|$.

The circumference c of each concentric circle before and after each stretch is then

$$c_{before} = 2\pi\left|\rightarrow \rho_r\right|$$

$$c_{after} = 2\pi\left|\rightarrow \rho'_r\right|$$

and the ratio represents the circumferential strain, which is evaluated from $r=0$ (center of membrane) to r = a (at the edge of the membrane):

$$\varepsilon_c = \frac{\left|\vec{\rho'_r}\right| - \left|\vec{\rho}_r\right|}{\left|\vec{\rho}_r\right|}$$

Radial strain

The radial strain ε_r represents the change in length between pairs of points at different radial positions. This strain is calculated as the ratio of the distance between two points p_1 and p_2 before and after inflation. Let $\vec{x}\,i$, $\vec{y}\,i$, and $\vec{z}\,i$ be the three-dimensional Cartesian position vectors of p1 and p2 before inflation. The same vectors after inflation are noted with a'. The radial strain is then

$$\varepsilon_r = \frac{\left|\left(\vec{x'_2} - \vec{x'_1}\right) + \left(\vec{y'_2} - \vec{y'_1}\right) + \left(\vec{z'_2} - \vec{z'_1}\right)\right| - \left|\left(\vec{x_2} - \vec{x_1}\right) + \left(\vec{y_2} - \vec{y_1}\right) + \left(\vec{z_2} - \vec{z_1}\right)\right|}{\left|\left(\vec{x_2} - \vec{x_1}\right) + \left(\vec{y_2} - \vec{y_1}\right) + \left(\vec{z_2} - \vec{z_1}\right)\right|}$$

References

Arnsdorf EJ, Tummala P, Kwon RY, Jacobs CR. Mechanically induced osteogenic differentiation–the role of RhoA, ROCKII and cytoskeletal dynamics. J Cell Sci. 2009; 122:546–553. [PubMed: 19174467]

Balestrini JL, Skorinko JK, Hera A, Gaudette GR, Billiar KL. Applying controlled non-uniform deformation for in vitro studies of cell mechanobiology. Biomech Model Mechanobiol. 2010; 9:329–344. [PubMed: 20169395]

Benedek G. Theory of transparency of the eye. Appl Opt. 1971; 10:459–473. [PubMed: 20094474]

Butler DL, et al. Using functional tissue engineering and bioreactors to mechanically stimulate tissue-engineered constructs. Tissue Eng A. 2009; 15:741–749.

Case ND, Duty AO, Ratcliffe A, Müller R, Guldberg RE. Bone formation on tissue-engineered cartilage constructs in vivo: effects of chondrocyte viability and mechanical loading. Tissue Eng. 2003; 9:587–596. [PubMed: 13678438]

Coulombre AJ, Coulombre JL. The role of intraocular pressure in the development of the chick eye: IV. Corneal curvature. Arch Ophthalmol. 1958; 59:502.

Coulombre AJ, Coulombre JL. Corneal development. I. Corneal transparency. J Cell Comp Physiol. 2005; 51:1–11.

Cox J, Farrell R, Hart R, Langham M. The transparency of the mammalian cornea. J Physiol. 1970; 210:601–616. [PubMed: 5499815]

Dartsch P, Hämmerle H. Orientation response of arterial smooth muscle cells to mechanical stimulation. Eur J Cell Biol. 1986; 41:339. [PubMed: 3530766]

Dartsch P, Hämmerle H, Betz E. Orientation of cultured arterial smooth muscle cells growing on cyclically stretched substrates. Cells Tissues Organs. 1986; 125:108–113.

Duty AO, Oest ME, Guldberg RE. Cyclic mechanical compression increases mineralization of cell-seeded polymer scaffolds in vivo. J Biomech Eng. 2007; 129:531–539. [PubMed: 17655474]

Eastwood M, McGrouther D, Brown R. Fibroblast responses to mechanical forces. Proc Inst Mech Eng H J Eng Med. 1998; 212:85–92.

Gupta V, Grande-Allen KJ. Effects of static and cyclic loading in regulating extracellular matrix synthesis by cardiovascular cells. Cardiovasc Res. 2006; 72:375–383. [PubMed: 17010955]

Jester JV, Ho-Chang J. Modulation of cultured corneal keratocyte phenotype by growth factors/cytokines control in vitro contractility and extracellular matrix contraction. Exp Eye Res. 2003; 77:581–592. [PubMed: 14550400]

Kamotani Y, et al. Individually programmable cell stretching microwell arrays actuated by a Braille display. Biomaterials. 2008; 29:2646–2655. [PubMed: 18342367]

Kanda K, Matsuda T. Mechanical stress-induced orientation and ultra-structural change of smooth muscle cells cultured in three-dimensional collagen lattices. Cell Transplant. 1993; 3:481–492.

Kanda K, Matsuda T, Oka T. Mechanical stress induced cellular orientation and phenotypic modulation of 3-D cultured smooth muscle cells. ASAIO J. 1993; 39:M691. [PubMed: 8268626]

Karamichos D, Lakshman N, Petroll WM. Regulation of corneal fibroblast morphology and collagen reorganization by extracellular matrix mechanical properties. Investig Ophthalmol Vis Sci. 2007; 48:5030–5037. [PubMed: 17962454]

Kim BS, Nikolovski J, Bonadio J, Mooney DJ. Cyclic mechanical strain regulates the development of engineered smooth muscle tissue. Nat Biotechnol. 1999; 17:979–983. [PubMed: 10504698]

Lee WCC, Maul TM, Vorp DA, Rubin J, Marra KG. Effects of uniaxial cyclic strain on adipose-derived stem cell morphology, proliferation, and differentiation. Biomech Model Mechanobiol. 2007; 6:265–273. [PubMed: 16906436]

Li H, Jang J, Cai S. Fabrication of microfluidic systems in poly (dimethylsiloxane). Polym Bull. 2005; 01

MacKenna D, Summerour SR, Villarreal FJ. Role of mechanical factors in modulating cardiac fibroblast function and extracellular matrix synthesis. Cardiovasc Res. 2000; 46:257–263. [PubMed: 10773229]

Maurice DM. The structure and transparency of the cornea. J Physiol. 1957; 136:263. [PubMed: 13429485]

McBeath R, Pirone DM, Nelson CM, Bhadriraju K, Chen CS. Cell shape, cytoskeletal tension, and RhoA regulate stem cell lineage commitment. Dev Cell. 2004; 6:483–495. [PubMed: 15068789]

Moraes C, Chen JH, Sun Y, Simmons CA. Microfabricated arrays for high-throughput screening of cellular response to cyclic substrate deformation. Lab Chip. 2009; 10:227–234. [PubMed: 20066251]

Moraes C, Chen JH, Sun Y, Simmons CA. Microfabricated arrays for high-throughput screening of cellular response to cyclic substrate deformation. Lab Chip. 2010; 10:227–234. [PubMed: 20066251]

Moraes C, Sun Y, Simmons CA. (Micro)managing the mechanical microenvironment. Integr Biol. 2011; 3:959–971.

Moraes C, et al. Microdevice array-based identification of distinct mechanobiological response profiles in layer-specific valve interstitial cells. Integr Biol. 2013; 5:673–680.

Nirmalanandhan VS, et al. Effect of scaffold material, construct length and mechanical stimulation on the in vitro stiffness of the engineered tendon construct. J Biomech. 2008; 41:822–828. [PubMed: 18164020]

Palomares KTS, et al. Mechanical stimulation alters tissue differentiation and molecular expression during bone healing. J Orthop Res. 2009; 27:1123–1132. [PubMed: 19242967]

Paten JA, Zareian R, Saeidi N, Melotti SA, Ruberti JW. Design and performance of an optically accessible, low-volume, mechanobioreactor for long-term study of living constructs. Tissue Eng C Methods. 2011; 17:775–788.

Quinlan AMT, Sierad LN, Capulli AK, Firstenberg LE, Billiar KL. Combining dynamic stretch and tunable stiffness to probe cell mechanobiology in vitro. PLoS ONE. 2011; 6:e23272. [PubMed: 21858051]

Rabinowitz YS. Keratoconus. Sur Opthalmol. 1998; 42:297–319.

Rezakhaniha R, et al. Experimental investigation of collagen waviness and orientation in the arterial adventitia using confocal laser scanning microscopy. Biomech Model Mechanobiol. 2012; 11:461–473. [PubMed: 21744269]

Ruberti JW, Zieske JD. Prelude to corneal tissue engineering–gaining control of collagen organization. Prog Retin Eye Res. 2008; 27:549–577. [PubMed: 18775789]

Ruggiero F, Burillon C, Garrone R. Human corneal fibrillogenesis. Investig Ophthalmol Vis Sci. 1996; 37

Saeidi N, et al. Disorganized collagen scaffold interferes with fibroblast mediated deposition of organized extracellular matrix in vitro. Biotechnol Bioeng. 2012; 109:2683–2698. [PubMed: 22528405]

Screen HR, Shelton JC, Bader DL, Lee DA. Cyclic tensile strain upregulates collagen synthesis in isolated tendon fascicles. Biochem Biophys Res Commun. 2005; 336:424–429. [PubMed: 16137647]

Wang JHC, Thampatty BP. An introductory review of cell mechanobiology. Biomech Model Mechanobiol. 2006; 5:1–16. [PubMed: 16489478]

Wang J, Chen H, Seth A, McCulloch CA. Mechanical force regulation of myofibroblast differentiation in cardiac fibroblasts. Am J Physiol Heart Circ Physiol. 2003a; 285:H1871–H1881. [PubMed: 12842814]

Wang JHC, et al. Cyclic mechanical stretching of human tendon fibroblasts increases the production of prostaglandin E 2 and levels of cyclooxygenase expression: a novel in vitro model study. Connect Tissue Res. 2003b; 44:128–133. [PubMed: 14504032]

Williams B. Mechanical influences on vascular smooth muscle cell function. J Hypertens. 1998; 16:1921–1929. [PubMed: 9886878]

Winkler M, et al. Nonlinear optical macroscopic assessment of 3-D corneal collagen organization and axial biomechanics. Investig Ophthalmol Vis Sci. 2011; 52:8818–8827. [PubMed: 22003117]

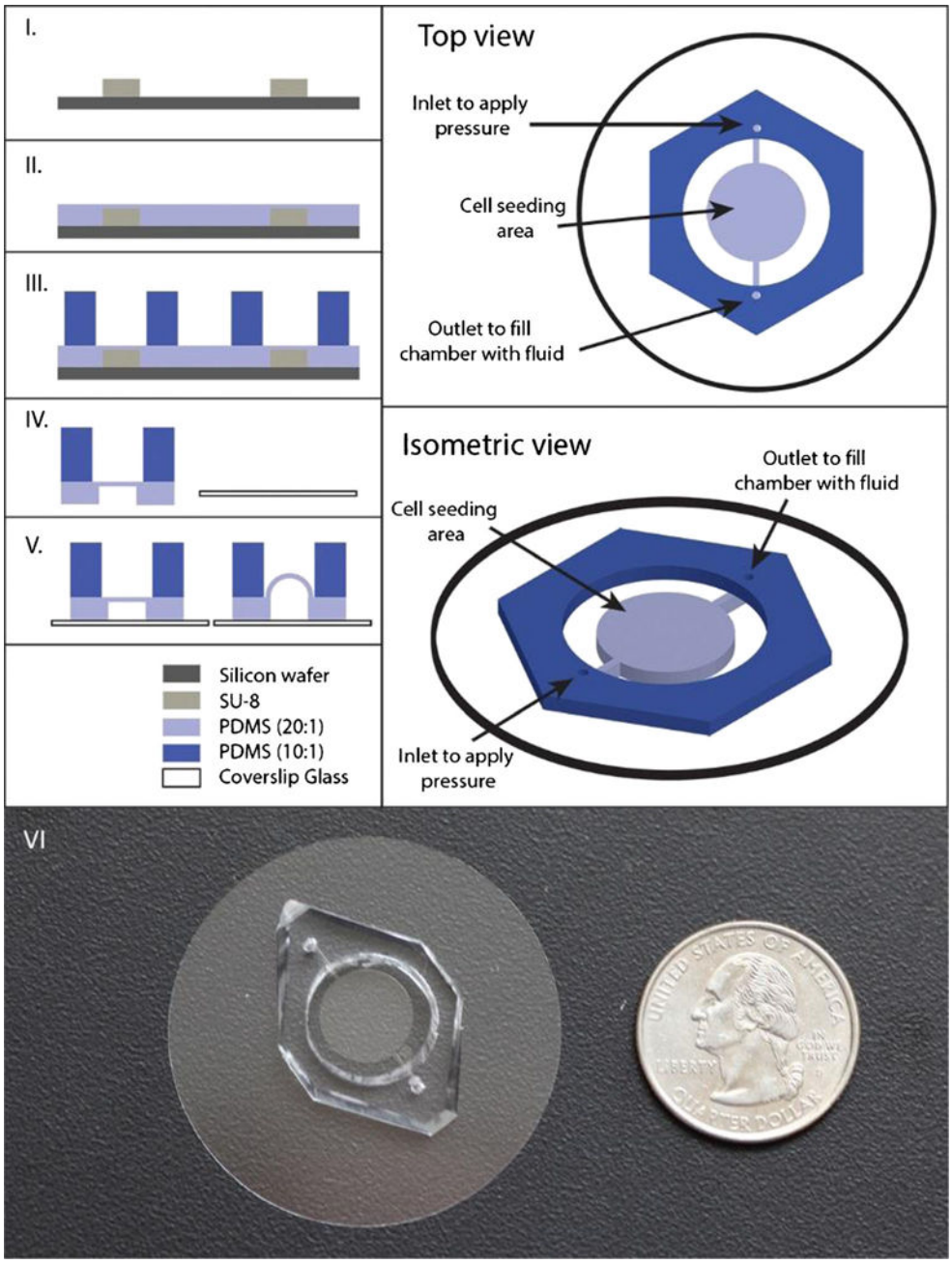

Fig. 1.

(*Left*) Step-by-step fabrication process of the microfabricated devices, shown from a side view. *I.* SU-8 is patterned using traditional photolithography processes to a height of 100 μm. *II.* PDMS with a base: curing agent ratio of 20:1 (w/w) is spun onto the SU-8 mold, forming a thin membrane over the SU-8 features. *III.* A 4 mm thick "handle layer" of PDMS is plasma bonded to the thin PDMS membrane. A 12 mm diameter hole is punched and aligned over the 10 mm diameter membrane area where cells will be seeded. *IV.* The two-layer PDMS device is cut from the SU-8 mold and plasma-bonded to a circular glass cover slip. *V.* The device is shown in the relaxed (*left*) and inflated (*right*) states. By applying

pressure through the microfabricated channel in the device, the thin PDMS membrane deflects upward, inducing strain on the surface of the membrane. The thickness of the 10:1 PDMS layer provides space for cell culture media, allowing for extended studies using the platform. (*Right*) Top and isometric views of the assembled device are shown, along with major features, including the inlet and outlet for the microfabricated channel, and the membrane area, where cells will be cultured. *VI.* Photograph of the device

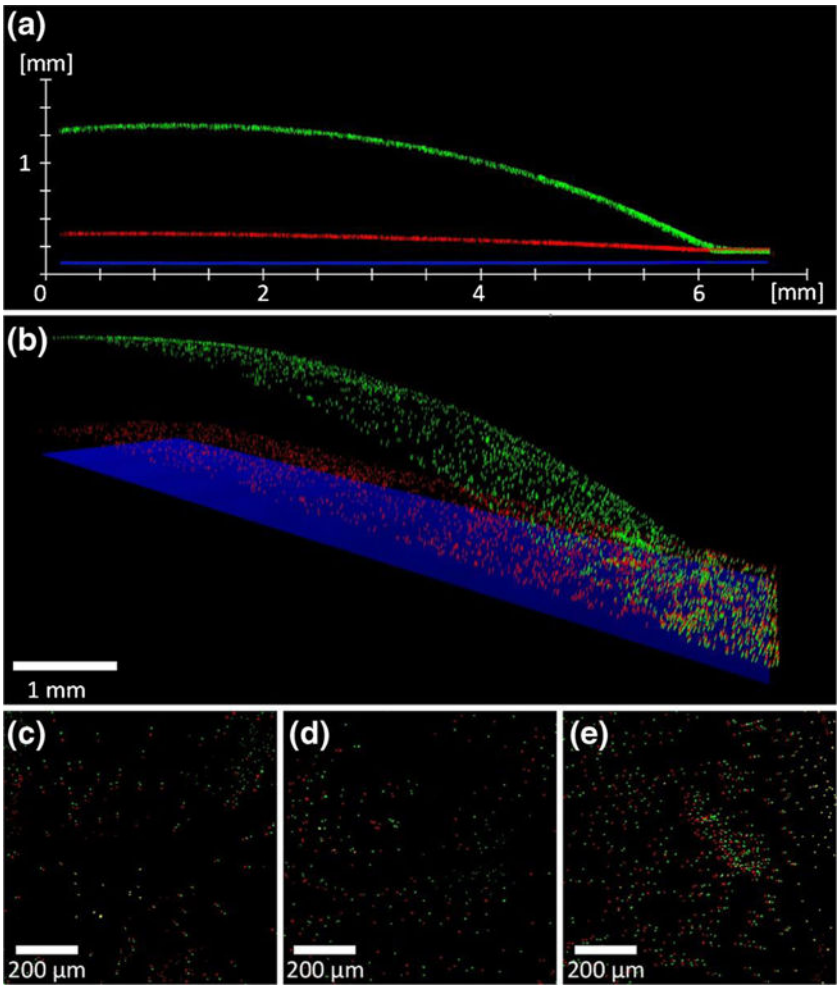

Fig. 2.

Membrane deflection visualized using fluorescent polystyrene microbeads. (**a**) Hybrid cross-sectional view of the device showing two inflation states: relaxed (*red*) and pressurized (*green*). The glass device base is shown in *blue*. The deformation is best appreciated using 3-D renders (**b**) which show the combined in-plane and vertical displacement. (**c**)–(**e**) Overhead views from selected regions show in-plane deflection. *Red dots* indicate bead positions in the relaxed state, *green dots* show bead positions after the device was pressurized. Near the center (**c**), deflection is minimal, causing only slight bead movement. With increasing distance from the center, bead separation increases (**d**), indicating large amounts of in-plane stretch. At the periphery, bead separation is minimal (**e**)

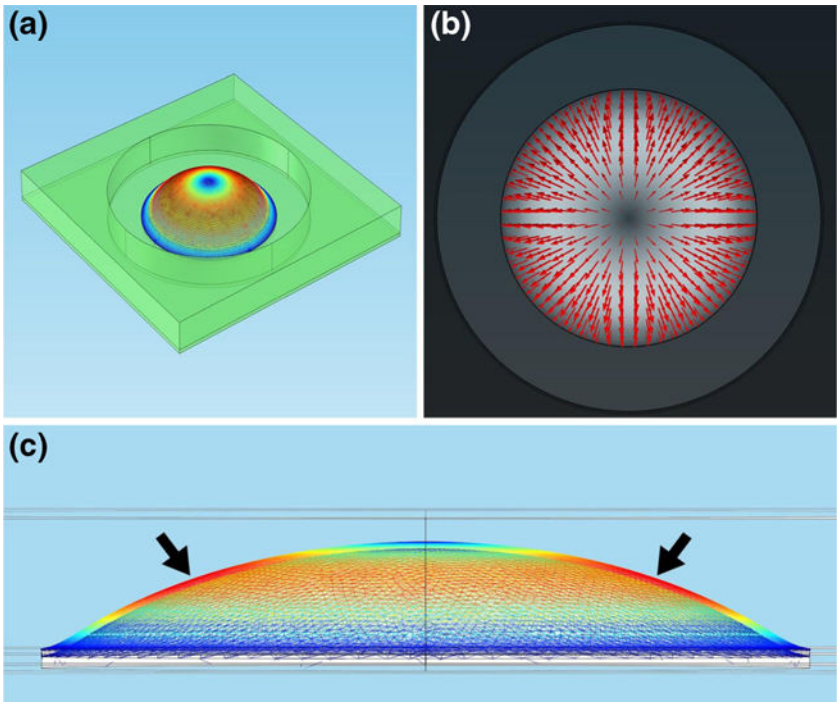

Fig. 3.

Finite element simulations of the device show membrane deformation and membrane stresses. **a** Isometric view of the device color-coded for in-plane displacement. **b** Top-down vector field view showing the major directions of in-plane strain. **c** Side-view color-coded for in-plane displacement. Areas of maximum displacement are shown in *dark red* (*black arrows*)

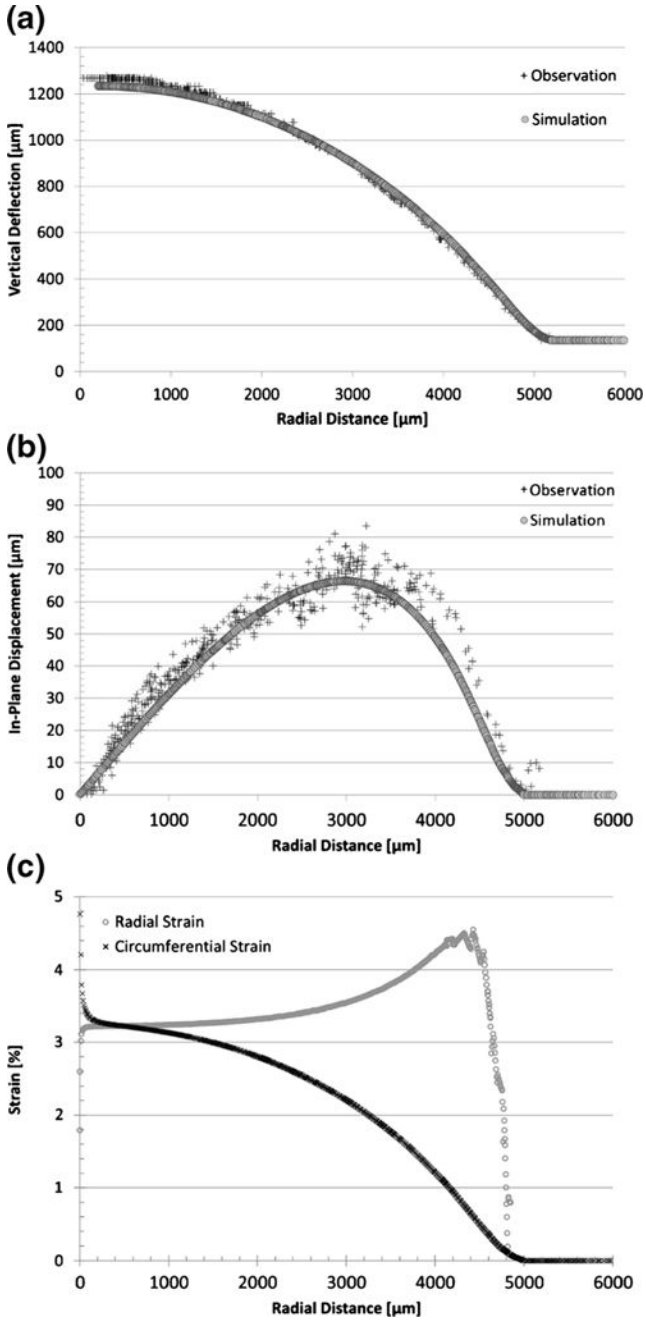

Fig. 4.

Comparison of membrane deflection with finite element predictions. **a** vertical deflection measured by 3-D measurement of fluorescent bead positions (+) and corresponding predictions from the finite element simulation (o). **b** In-plane (x/y) displacement of beads (+) and corresponding data from finite element simulation (o). **c** Radial (o) and circumferential (x) strain calculated based on membrane deflection plotted as a function of radial distance

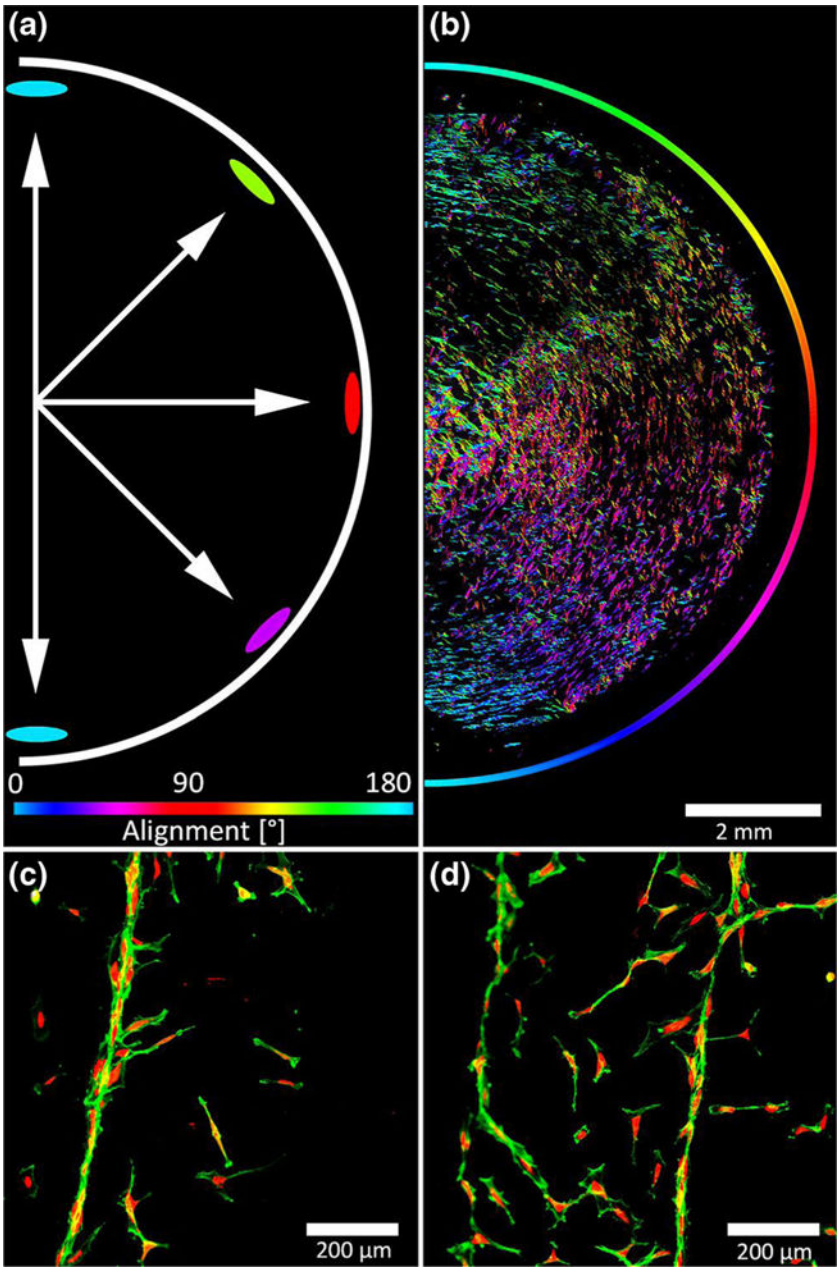

Fig. 5.

(**a**) Major stretch directions (*arrows*) and predicted cell alignment (*ovals*) color-coded for angle. In this coordinate system, 0° corresponds to the 3 o'clock position, 90° is at the 12 o'clock position. Cells are predicted to align perpendicular to the in-plane stretch (*white arrows*). (**b**) Actual cell alignment measured by the OrientationJ color survey module applied to a fluorescent image of rabbit corneal cells after 36 h of cyclical stretch at 500 mHz. Cells were stained with phalloidin for actin and with DAPI to visualize nuclei. The color-coding corresponds to the one used in (**a**). (**c**) and (**d**): High-resolution confocal microscopy images of aligned cells post-stretch stained with phalloidin (actin, *green*) and DAPI (nuclei, *red*)

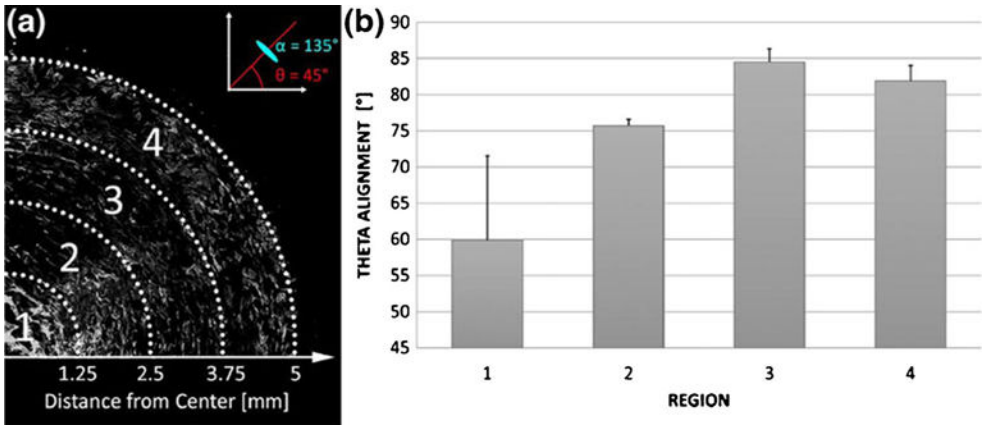

Fig. 6.

a Images were divided into four concentric regions and alignment was quantified by running the OrientationJ quantification module repeatedly on consecutive ROIs radiating outward from the device center. **b** OrientationJ quantification results expressed as theta alignment. The predominant orientation for each region of interest expressed as a function of the angular component of each region's polar coordinates averaged and divided into four radial groups shown in (**a**). Inset defines coordinates for calculations. A value of 90° indicates alignment perpendicular to the radius vector, while 0° corresponds cell alignment parallel to the radius vector. Avalue of 45°, combined with high standard error values, signifies near-random alignment of cells whereas small errors indicate that the vast majority of cells are aligned along the preferential direction

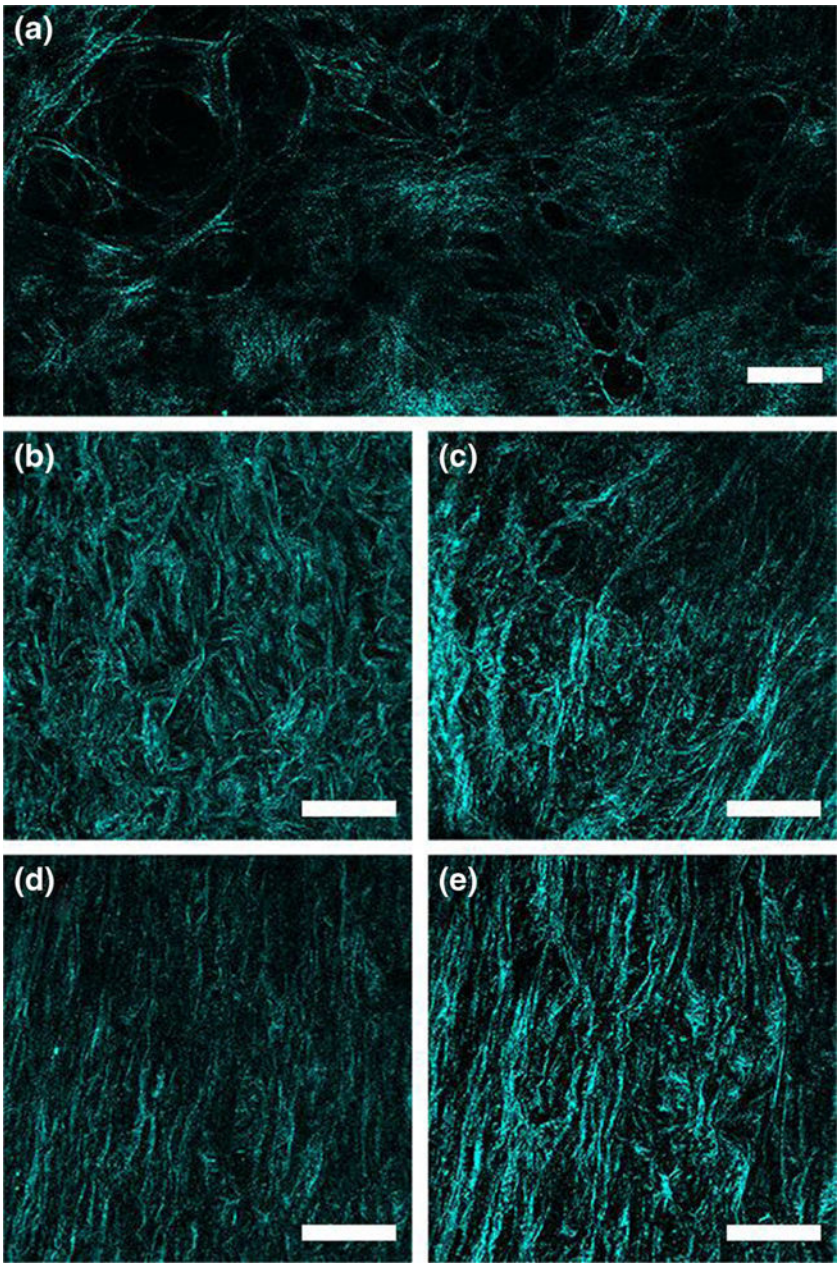

Fig. 7.

(**a**) Second Harmonic Generation (SHG) images of a *de novo* collagenous matrix synthesized by rabbit corneal cells cultured under serum-free conditions. This image is a composite of multiple high-resolution images taken after week 4. Close-up views of an area near the device center after 24 h (**b**) and 48 h (**c**) of cyclical stretch at 0.5 Hz. Corresponding views of an area approximately 3 mm from the device center after 24 h (**d**) and 48 h (**e**) show increased alignment of collagen fibers along a preferential direction